Estimation of land surface temperature retrieved from EOS/MODIS in Naqu area over Tibetan Plateau

WANG Binbin[1, 2, 3], MA Yaoming[1, 3], MA Weiqiang[2, 3, 4]

1. *Institute of Tibetan Plateau Research*, *Chinese Academy of Sciences*, *Beijing* 100085, *China*;
2. *Graduate University of Chinese Academy of Sciences*, *Beijing* 100049, *China*;
3. *Key Laboratory of Tibetan Environment Changes and Land Surface Processes*, *Chinese Academy of Sciences*, *Beijing* 100085, *China*;
4. *Cold and Arid Regions Environmental and Engineering Research Institute*, *Chinese Academy of Sciences*, *Lanzhou* 730000, *China*

Abstract: Using split window algorithms developed by Sobrino, added a sufficient and simple cloud detection process for MODIS L1B data. Then based on land surface classification (land, water, snow & ice), retrieved four land surface temperature images for clear sky in Naqu area over Tibetan Plateau in January, April, June and October in 2007, respectively. After that the derived LST was compared with the MODIS daily land surface temperature product and in-situ data from the Coordinated Enhanced Observing Period (CEOP) Asia-Australia Monsoon Project (CAMP) on Tibetan Plateau (CAMP/Tibet). The results showed that the LST derived from the improved Sobrino method was in good accordance with the MODIS product and the average difference between LST and in-situ measurements was only 1.435 K.

Key words: Tibetan Plateau, MODIS, split window algorithm, cloud detection, land surface temperature

CLC number: P423.7 **Document code:** A

Citation format: Wang B B, Ma Y M and Ma W Q. 2012. Estimation of land surface temperature retrieved from EOS/MODIS in Naqu area over Tibetan Plateau. Journal of Remote Sensing, 16(6): 1289–1309

1 INTRODUCTION

Well-known for the features of highest average altitude, largest area and most complex terrain in the word, Tibetan Plateau (TP) is referred to as the "Third Pole of the Earth" (Qiu, 2008). Because of its high topographic feature, it has significant influences on Asia monsoon, atmospheric circulation in East Asia and Global Climate Change (GCC) in land-atmosphere interactions and especially in energy water cycle progress (Ma, et al., 2004). Many large-scale field observation experiments have been carried out in research of land surface, atmosphere and their interactions (Chen, et al., 2008), such as "The First Tibetan Plateau Experiment", "The Second Tibetan Plateau Experiment of Atmospheric Science", "Global Energy and Water Cycle Experiment(GEWEX) and the Asia Monsoon Experiment on the TP (GAME/Tibet)", "the Coordinated Enhanced Observing Period (CEOP) Asia-Australia Monsoon Project on the TP (CAMP/Tibet)". Because of its harsh environment, the field observation data are still lacking limited by the sparse observation stations. Remote sensing technology will be one of the most important methods in obtaining land surface parameters.

In the research of land-atmosphere interactions, land surface temperature (LST) is a basic parameter which is defined as molecular motion temperature differed from the radiation temperature from satellite thermal infrared sensors (Zhao, 2003). LST is a key parameter in the research of land surface physical processes at regional and global scale and affects the results of land-atmosphere interaction and energy exchanges (Zhu, 2008). Traditional measurement methods can only obtain LST at point or local scales. The requirement for LST at regional or even global scale in environmental studies and resource managements makes remote sensing of LST an important research subject (Yang & Yang, 2006). In the last twenty years, LST retrieved from remote sensing made a big progress and split window algorithms (SWAs) are most popularly used. Based on the radiation transfer equation, with different atmospheric absorption effect of two adjacent channels in the atmospheric window in 10-13 micron, SWAs can remove the atmospheric effect and finally get the atmosphere emissivity and land surface emissivity (Zhao, 2003). Using the thermal infrared channel, Price (1984) first applied the SWAs to the crop land. Afterwards, Becker and Li (1990), Sobrino and Caselles (1991), Kerr, et al. (1992),

Received: 2011-10-11; **Accepted:** 2012-05-08

Foundation: ESA-MOST Dragon Cooperation Project (No.2010CB951701); National Science Found for Distinguished Young Scholars of China (No.40825015); The Knowledge Innovation Program of the Chinese Academy of Sciences (No.KZCX2-YW-QN309)

First author biography: WANG Binbin (1986—), male, Ph.D. candidate, he majors in the research of atmosphere boundary layer and application of remote sensing. E-mail: wangbinbin@itpcas.ac.cn

Corresponding author biography: MA Yaoming (1964—), male, professor, his research interests are atmosphere boundary layer and applications of remote sensing. E-mail: ymma@itpcas.ac.cn

Sobrino, et al. (1994), Coll and Caselles (1997), Sobrino and Raissouni (2000), Ma, et al. (2002), Sobrino, et al. (2003), Mao, et al. (2005) all contributed to the research of SWAs in retrieving LST. Among them, the development of "Sobrino LST inversion method" (Sobrino LST method) lasts longer with a better architecture and its inversion operation process is relatively simple.

The first EOS (Earth Observing System) morning orbiting satellite TERRA launched on December 18th in 1999, and MODIS is the most important instrument. With the features of global free, a large coverage area and 36 spectral bands, the MODIS data can greatly improve the spectral resolution and enhance the capabilities to observe the complex earth system and to identify surface types (Liu & Yang, 2001). In this paper, Sobrino LST method, after appropriate improvements, was applied to the Tibetan Plateau (TP) with MODIS L1B data. After that the derived LST was compared with the MODIS daily land surface temperature product and analyzed with in-situ data in Naqu area. Finally, we discussed its accuracy on TP.

2 DATA

2.1 MODIS data

In this paper, we used the HDF format MOIDS L1B data (MOD021KM-Level 1B Calibrated Radiance-1 km Terra satellite data) on 3rd January, 18th April, 12nd June and 2nd October. During the four chosen days, the area of sky cloud-cover was small on whole TP and it was convenient to validate with the ground observation data[1]. Those download data have been instrument calibrated but without atmospheric correction. We have to convert the DN value to radiance using the following equation. L_i=$scales_i$ × ($count_i$–$offset_i$), where L_i, $scales_i$, $scales_i$, $offset_i$ were radiance, scale factor, DN value and offset of band i respectively.

2.2 MODIS LST product

NASA data services web site[2] provides the MODIS/Terra Land Surface Temperature/ Emissivity Daily L3 Global 1 km SIN Grid v005 product which can be used as preliminary validation with Sobrino inversion LST result (LST RESULT). The physical-based day/night LST algorithm was used for the product (Wan & Li, 1997). And the product had been validated within 1 K precision in relatively wide ranges of surfaces and atmospheric conditions (Wan, et al., 2004). Before the verification, projection conversion and image mosaic were performed using MODIS Re-projection Tools (MRT).

2.3 Field observation data

The field observation data came from CAMP/Tibet experiment observation sites (including NPAM, BJ, D105 and Amdo). Aiming at understanding the energy exchange between surface and atmosphere of TP, GAME/Tibet program set a large number of observing stations in a 150 km×200 km area in Naqu on northern TP. The underlying surface contained plateau meadow, highland lake, desert steppe and so on. At the end of the project, it joined CEOP organized by GEWEX and Climate Variability and Predictability (CLIVAR) and started the CAMP/Tibet research. The original stations and the newly added stations started continuous observation and obtained very valuable data (Ma, et al., 2006).

The surface condition of the four observing sites are as below (Ma, et al., 2002; Ma, et al., 2005; Yang, et al., 2008): NPAM station (91°72'E, 31°93'N) shows a very flat ground with relative height of about 100—200 m hills distributed at east of about 5 km, west of about 30 km and north and south of about 10 km and the coverage of the ground is meadow; BJ station (91°54'E, 31°22'N) has an open location and the ground is covered by meadow; D105 station (91°94'E, 33°06'N) has a very flat ground and a very open view with hills standing at east direction of about 20 km away and the ground cover vegetation is meadow; Amdo station (91°37'E, 32°14'N) has a relatively smooth surface with a very open view and the ground is covered by plateau sparse meadow. The topography and surface characteristics of the selected observation sites make meteorological observation data represent the average condition of each site and their surrounding areas. Four sites are all equipped with surface radiation thermometer HR1-FL, two Pt/100 thermometers at the depth of the 0 cm and four-component radiation instruments, respectively. The upward and downward shortwave and long-wave radiation table of D105, NPAM and Amdo stations are Kipp & Zonenn Pyrammeter CM21 and the upward and downward height of the probe are 1.58 m and 1.28 m, respectively. Sampling time of radiation instrument on NPAM and D105 is 1 h while that of Amdo is 30 min. In BJ station, the upward and downward long-wave and shortwave radiation instruments are Eppley PIR and EKO MS-801. The height of the instruments is 1.5 m and the sampling time is 10 min.

With the upward and downward long-wave radiation data from the four stations mentioned above, LST can be calculated. By integrating LST data from various observational instruments, LST with large deviations can be excluded. Through linear interpolation with time, reliable LST validation data can be obtained. The inversion formula with long-wave radiation is shown in Eq. (1) (Yang, et al., 2008).

$$R_{\mathrm{lw}}^{\uparrow} = (1-\varepsilon_s)R_{\mathrm{lw}}^{\downarrow} + \varepsilon_s \sigma T_{\mathrm{g}}^{4} \tag{1}$$

where T_{g} is surface skin temperature; $R_{\mathrm{lw}}^{\uparrow}$ is upward long-wave radiation; $R_{\mathrm{lw}}^{\downarrow}$ is downward long-wave radiation; $\sigma = 5.67 \times 10^{-8}\mathrm{W{\cdot}m^{-2}K^{-4}}$ which is Stephen Boltzmann constant; ε_s is surface emissivity. Considering the meadow-based ground surface and the paper written by Yang (2008), we can set it equal to 0.9800.

3 METHODOLOGY

The key factors of SWAs are the calculation of surface emissivity, water vapor content (WVC) and brightness temperature of thermal infrared band in cloud-free atmosphere. Section 3.2—Section 3.5 show the details about the processing of the above 3 factors. And the overall process of the algorithm is shown in Fig. 1.

3.1 Data preprocess

MODIS L1B data were processed with the following pretreatments: (1)Geographical coordinate location information (latitude and longitude values taken from the positioning of geographical coordinates in the header file) was added to the original L1B data. (2)Overlap of the pixel at the edge of the image was removed by bowtie processing. (3)Based on radiation transfer calculation

[1] [2010-08-15] https://ladsweb.nascom.nasa.gov/index.htm
[2] [2010-09-15] https://wist.echo.nasa.gov/api/

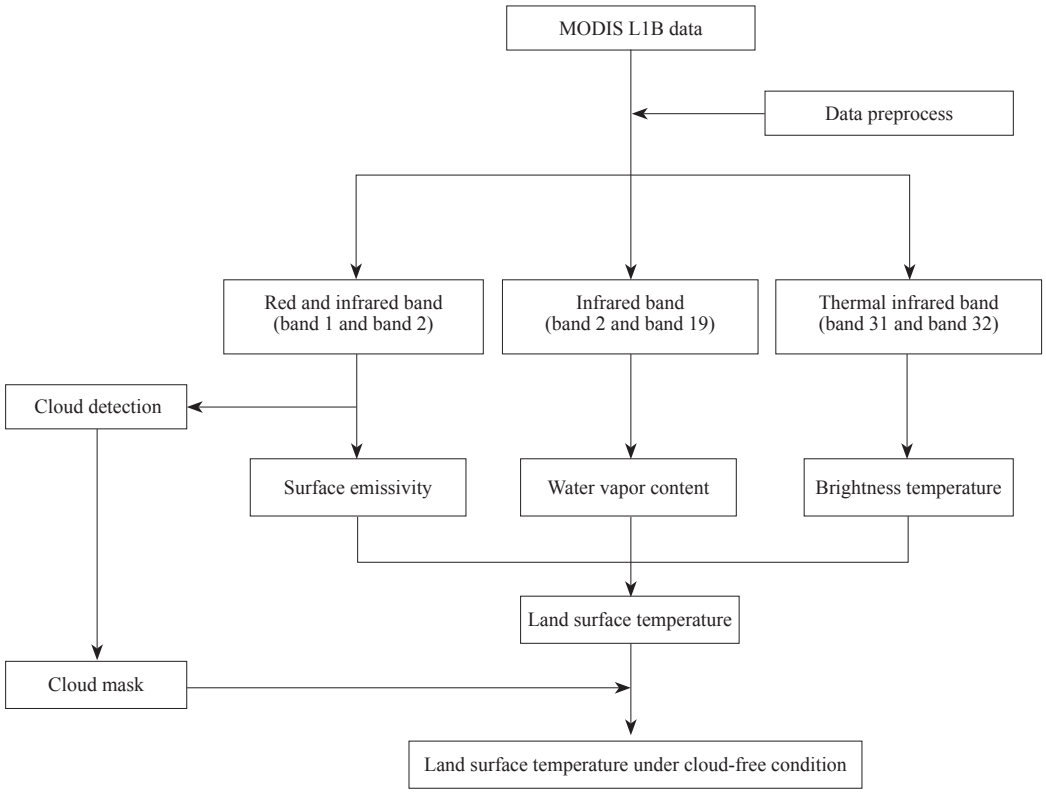

Fig. 1 Flowchart of MODIS LST estimation method

module MODerate spectral resolution atmospheric TRANSsmittance algorithm and computer model 4.0 (MODTRAN4.0) which is integrated in Fast Line-of-sight Atmospheric Analysis of Spectral Hypercubes (FLAASH) module, atmospheric calibration was done to remove the effects of atmospheric water vapor, carbon dioxide, methane, ozone and atmospheric molecular and aerosol scattering on surface reflectance. Correction results were used in calculating normalized difference vegetation index (NDVI) and the threshold value for cloud detection. We used the remote sensing image processing software (ENVI+IDL) to carry out the above processes.

3.2 Cloud detection

SWAs was based on the thermal radiation transfer equation under cloud-free and local thermal balance condition. So, cloud detection process was needed at first. The cloud-free detection method for AVHRR was developed by Saunders and Kriebel (1988). Based on the theory and the method of manual identity we could pick out the pixels without cloud and finally use them in retrieving LST. (1) The first test was an infrared threshold test: clouds have a greater optical depth in 12 μm brightness temperature. If the measured brightness temperature was below a certain threshold temperature (e.g. $T_{32} < 280$ K), the pixel was rejected as cloud-contaminated. (2) The second test used the ratio of near-infrared bidirectional reflectance to visible bi-directional reflectance Q. Over cloud-free water, enhanced backscattering at shorter wavelengths due to molecular and aerosol scattering caused the visible reflectance to be often twice than that of near-infrared band, so Q was approximated by 0.5; Over land, the reflectance at visible wavelengths is far less than that at near-infrared reflectance, so Q is always greater than 1; Over the cloud or snow & ice, the reflectance for the two bands has no big difference, so Q was approximated by 1. So, $a_1 < \rho_{nir} / \rho_r < a_2$ was used as one condition to judge whether the pixel was covered by cloud or snow & ice. a_1 and a_2 can be obtained from the image. (3)Cloud should be distinguished from snow & ice. The reflectance of clouds at shortwave band is higher than that of snow & ice. So, the reflectance of band 6 ($\rho_6 > c$) can be used to distinguish cloud and snow & ice. Parameter c could be acquired from the image. The pixels that fulfill all the three tests can be considered as cloud-contaminated. Through this process, images could be classified into land, water, cloud and snow & ice.

3.3 Calculation of brightness temperature

Plank's law links the spectral radiance emitted by a blackbody at a given wavelength and temperature in Eq. (2).

$$B_\lambda(T) = 2hc^2\lambda^{-5} \times [\exp(hc / \lambda kT) - 1]^{-1} \quad (2)$$

where $B_\lambda(T)$ is the spectral radiance of the blackbody; h is Plank's constant; c is the speed of light; λ is the wavelength, k is Boltzmann's constant, T is temperature in Kelvin. By inverting the Planck's radiation equation (Qin, et al., 2001), we can get

$$T = \frac{c_2}{\lambda \ln\left[\left(\frac{2c_1}{\lambda^5 B_\lambda(T)} + 1\right)\right]} \quad (3)$$

where c_1=5.95522012 × 10^{-17} W·m^2; c_2=1.43876869 × 10^{-2} m·K. Through Eq. (3) we can convert the radiance value to brightness temperature.

3.4 Calculation of emissivity

Land surface emissivity is not only connected with composition,

condition and physical character of the land surface but also related to band selection (Zhao, 2003). Although underlying surface is very complicated, it can be classified into vegetation, bare soil, water and snow & ice from the view of MODIS 1Km spatial resolution.

NDVI threshold method was developed by Sobrino in 2003 and it was used to estimate the emissivity of vegetation and bare soil (Sobrino, et al., 2003). The mean and difference emissivity can be obtained as below.

For mixed pixels ($0.2 < \mathrm{NDVI} < 0.5$) Eq. (4) and Eq. (5) are used.

$$\varepsilon = 0.971 + 0.018P_v \tag{4}$$

$$\Delta\varepsilon = 0.006(1 - P_v) \tag{5}$$

For pixels covered fully by vegetation ($\mathrm{NDVI} \geqslant 0.5$), Eq. (6) and Eq. (7) are used.

$$\varepsilon = 0.985 + d\varepsilon \tag{6}$$

$$\Delta\varepsilon = 0 \tag{7}$$

For bare soil ($\mathrm{NDVI} \leqslant 0.2$), Eq. (8) and Eq. (9) are shown as below.

$$\varepsilon = 0.9832 - 0.058\rho_1 \tag{8}$$

$$\Delta\varepsilon = 0.0018 - 0.060\rho_1 \tag{9}$$

where ρ_1 and ρ_2 are the spectral reflectance for MODIS band 1 and band 2; $d\varepsilon$=0.005; NDVI can be expressed as Eq. (10) and P_v is the vegetation coverage of the pixel (Carlson & Ripley, 1997) shown in Eq. (11).

$$\mathrm{NDVI} = \frac{\rho_2 - \rho_1}{\rho_2 + \rho_1} \tag{10}$$

$$P_v = \left(\frac{\mathrm{NDVI} - \mathrm{NDVI}_{\min}}{\mathrm{NDVI}_{\max} - \mathrm{NDVI}_{\min}}\right)^2 \tag{11}$$

In our research, $\mathrm{NDVI}_{\max}$ and $\mathrm{NDVI}_{\min}$ was set according to the type of surface characteristics of the study area. If there is obvious bare soil area, then take the average NDVI value of the bare soil as $\mathrm{NDVI}_{\min}$. If there is fully vegetation covered area, then take the average NDVI value of the vegetation as $\mathrm{NDVI}_{\max}$. Considering the actual condition of the four images in Naqu area, we set $\mathrm{NDVI}_{\max}$=0.55, $\mathrm{NDVI}_{\max}$=0.05.

Specific underlying surface such as glacier and lake exist on TP. For lake, because of water's single structure, the emissivity of water is always between 0.97 and 1.0. The emissivity of band 31 and 32 can be set 0.992 and 0.988, respectively (Mao, et al., 2005). So the average emissivity of water can be 0.990 and the difference emissivity can be 0.004. For snow & ice, Li (2005) pointed out that the emissivity in MODIS band 31 and 32 can be 0.988 and 0.977, so the average emissivity can be 0.9825 and the difference emissivity can be 0.11. Sobrino, et al. (2003) showed that the uncertainty of 0.005 in emissivity can only cause uncertainty of 0.64 K in LST result. So, the empirical emissivity mentioned above may lead to very small uncertainty in LST result.

3.5 Calculation of water vapor content

Kaufman and Gao (1992) performed many experiments and found that it is reasonable to retrieve the WVC of the atmosphere by ratio.

$$\tau_i = \rho_i / \rho_2 \tag{12}$$

where ρ_i (i=17, 18, 19) and ρ_2 represent the reflectance of bands i, 2 respectively; τ_i represents the transmittance of channel i. Kaufman and Gao gave Eq. (13) to calculate WVC (W) as follows.

$$\tau_i(19/2) = \exp(\alpha - \beta\sqrt{w}) \tag{13}$$

The correlation coefficient between transmittance (τ_i(19/2)) and WVC (W) was 0.999. For complex ground surface: α=0.02, β=0.65. So

$$W = \left(\frac{0.02 - \ln\tau_i}{0.65}\right)^2 \tag{14}$$

With the method and equations given above, we can calculate the mean emissivity, difference emissivity, brightness temperature of band 31, brightness temperature of band 32 and WVC for each pixel. So we can get LST using the Eq. (15) as

$$T_{\mathrm{sfc}} = T_{31} + 1.02 + 1.79\times(T_{31} - T_{32}) + 1.20\times(T_{31} - T_{32})^2 + (34.83 - 0.68W)(1-\varepsilon) + (-73.27 - 5.19W)\times\Delta\varepsilon \tag{15}$$

4 RESULTS AND VALIDATION

4.1 Comparison of WVC estimation method

WVC can be calculated by channel radiation ratio method (referred to as Sobrino method) developed by Sorbino, et al. (2003) or channel apparent reflectance ratio method (referred to as Kaufman method). Both Sobrino and Kaufman methods used the ratio of atmospheric window channel (MODIS band 2, band 5) and atmospheric water vapor absorption channel (MODIS band 17, band 18, band 19) to approximately describe the transmittance of the atmospheric water vapor absorption band. Then models were used to simulate the relationship between WVC and atmospheric transmittance. MODTRAN was used by Sobrino, et al. (2003) in simulating the relationship between radiance ratio and WVC while Kaufman, et al. (1992) used LOWTRAN to calculate the WVC.

GPS atmospheric WVC observation data from Japan International Cooperation Agency (JICA) project together with MODIS atmospheric WVC product are used to validate and evaluate the results retrieved from MODIS L1B data on January 6th and 7th 2008 over Tibetan Plateau and its surrounding area. The results are shown in Table 1, Table 2 and Fig. 2.

We can conclude from the scatter graph between inversion results of WVC (Fig. 2) that the results obtained from Sobrino

Table 1 The comparison of WVC (GPS value, MODIS product, Sorbrino Method, Kaufman method) on 6th January 2008 /cm

Sites	Longitude/ (°E)	Latitude/ (°N)	MODIS product	Sobrino method	Kaufman method	GPS value
Gerze	84.06221	32.30626	0.397	0.874	0.326	No data
Ganzi	99.99755	31.61966	0.253	0.882	0.319	0.3074
Nyingchi	94.36041	29.64812	0.548	0.484	0.748	No data
Takako	92.46006	28.41416	0.189	1.424	0.147	0.1415
Naqu	92.06118	31.47977	0.236	1.422	0.147	0.2073
Xainza	88.70490	30.93161	0.212	1.40	0.152	No data
Chamdo	97.17428	31.14696	0.248	0.996	0.270	No data
Dechen	98.90737	28.48851	0.187	0.932	0.296	0.2462
Dingqing	95.59356	31.41513	0.295	0.966	0.282	0.1734
Tingri	87.12039	28.65461	0.307	1.199	0.201	No data

Table 2 The comparison of WVC (GPS value, MODIS product, Sorbrino Method, Kaufman method) on January 7th 2008 /cm

Sites	Longitude/ (°E)	Latitude/ (°N)	MODIS product	Sobrino method	Kaufman method	GPS value
Lijiang	100.21865	26.84876	0.602	0.467	0.750	0.799
Dali	100.17593	25.70729	0.727	0.449	1.067	0.533
Ganzi	99.99755	31.61966	0.279	0.939	0.293	No data
Kunming	102.65295	25.00769	0.401	0.515	0.678	0.53
Nyingchi	94.36041	29.64812	0.588	0.446	0.949	0.74
Litang	100.27077	29.99468	0.333	1.143	0.219	0.444
Takako	92.46006	28.41416	0.420	0.612	0.526	0.342
Tengchong	98.49748	25.01855	0.782	0.447	1.056	0.919
Weining	104.28078	26.86327	0.388	0.642	0.481	No data
Xichang	102.26766	27.90411	0.881	0.493	1.369	0.776
Chamdo	97.17428	31.14696	0.291	1.021	0.261	No data
Dechen	98.90737	28.48851	0.432	0.745	0.4	0.514
Dingqing	95.59356	31.41513	0.396	0.769	0.387	No data

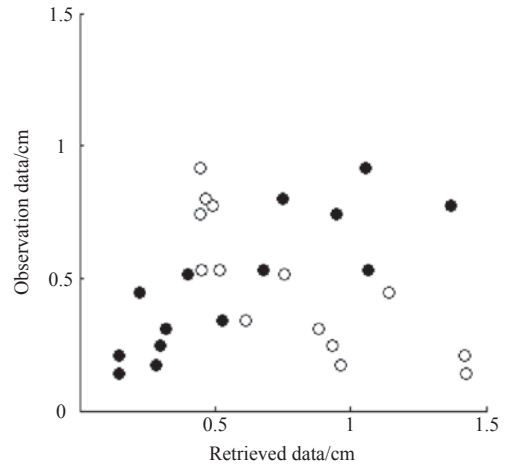

(a) Comparison with observation data

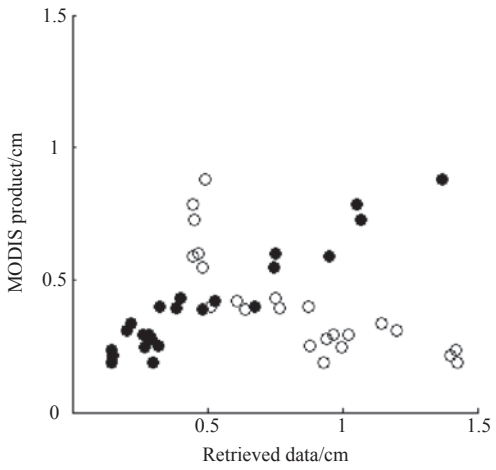

(b) Comparison with MODIS product

○ Sobrino ● Kaufman

Fig. 2 Scatter of atmospheric WVC

method (open circle) nearly has no regular pattern with GPS observed data while Kaufman method shows very ideal results. Meanwhile, the results obtained by Kaufman method are consistent with the MODIS product. So, the results from Kaufman method are more credible on TP and its surrounding area and original Sobrino method was replaced by Kaufman method in LST estimation method.

4.2 Validation with MODIS product

Fig. 3 and Fig. 4 show the histogram and spatial distribution of LST. Fig. 3 shows that the histograms from LST result and MODIS product have a very consistent feature. The same is seen for the spatial distribution of LST in Fig. 4. We can see from the four images that LST gradually decreased from south to north with the latitude increase in Naqu area. In Fig. 3, the Nam Co Lake area (April 18th) and Selin Co Lake area (June 12nd) were both detected as cloud-cover area in MODIS product. Snow & ice had very high reflectance in 0.555 μm (MODIS band 4, green band) and had low reflectance in 1.64 μm (MODIS band 6, shortwave infrared) while that of cloud is high in both two bands. So, we can use Normalized Difference Snow Index (NDSI) to distinguish cloud and snow & ice (Wang, et al., 2007). After verification with NDSI that with very high NDSI, visible reflectance was high while shortwave infrared reflectance was low. So, it was wrong to identify Nam Co Lake area as cloud in April. In our result, we considered it as snow & ice, which was consistent with the weather condition at that time. In June, NDSI in Selin Co lake area was low while shortwave infrared reflectance was also low. So, whether the area was covered by cloud needs more auxiliary information.

Table 3 shows the contrast of maximum, minimum and average value between LST RESULT and MODIS product (the maximum and minimum value taken from more than 10 pixels at the same interval as boundary value). The average temperature of the four images can also simply reflect the characteristics of seasonal variations of LST. Table 3 shows that the average differences of the four images are all less than 1 K and the biggest average difference value is only 0.79 K. On October 2nd 2007, the minimum difference was 13.02 K. It was because that we selected the simple threshold method in Section 3.2 to detect clouds, and the threshold was determined by artificial recognition. There are a large number of clouds in southeastern region on October 2nd. The pixels at the edge of the cloud may be misjudged by the method. So the minimum value (seen as cloud) of the statistical results was low.

The maximum difference between MODIS product and LST RESULT was –1.32 K on June 13rd 2007 and LST RESULT was a little higher. In the statistical analysis of LST, there existed a few high LST pixels whose total number was less than 10 and they had a relative high brightness difference between MODIS band 31 and band 32. From Eq. (15), LST was influenced significantly by the brightness difference from MODIS band 31 and band 32. The bigger brightness temperature difference of the two bands is, the higher the LST is. So, in the process of cloud detection, brightness difference should be considered as one important factor in the cloud-detection process.

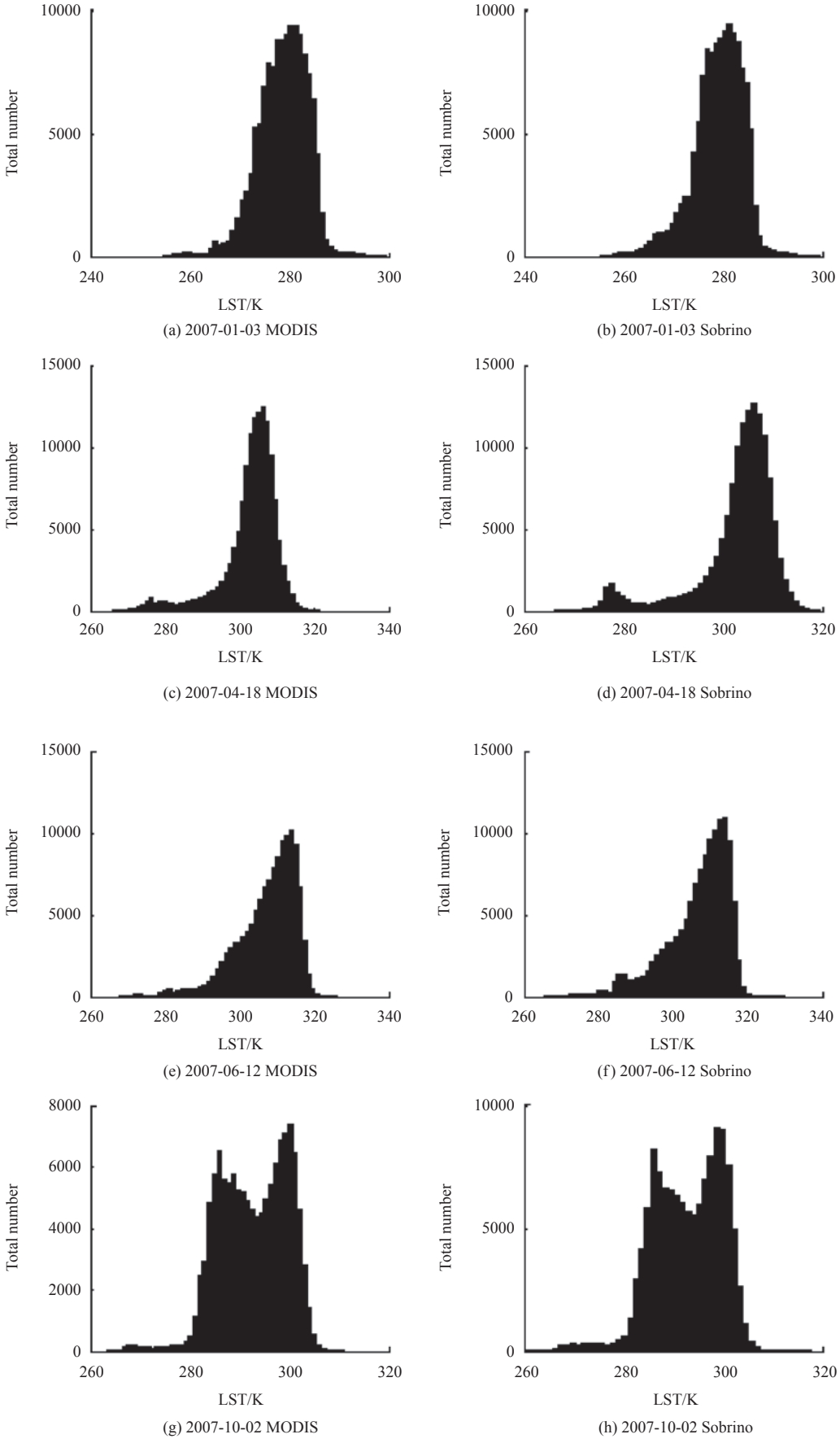

Fig. 3 Histogram of MODIS results and LST RESULT

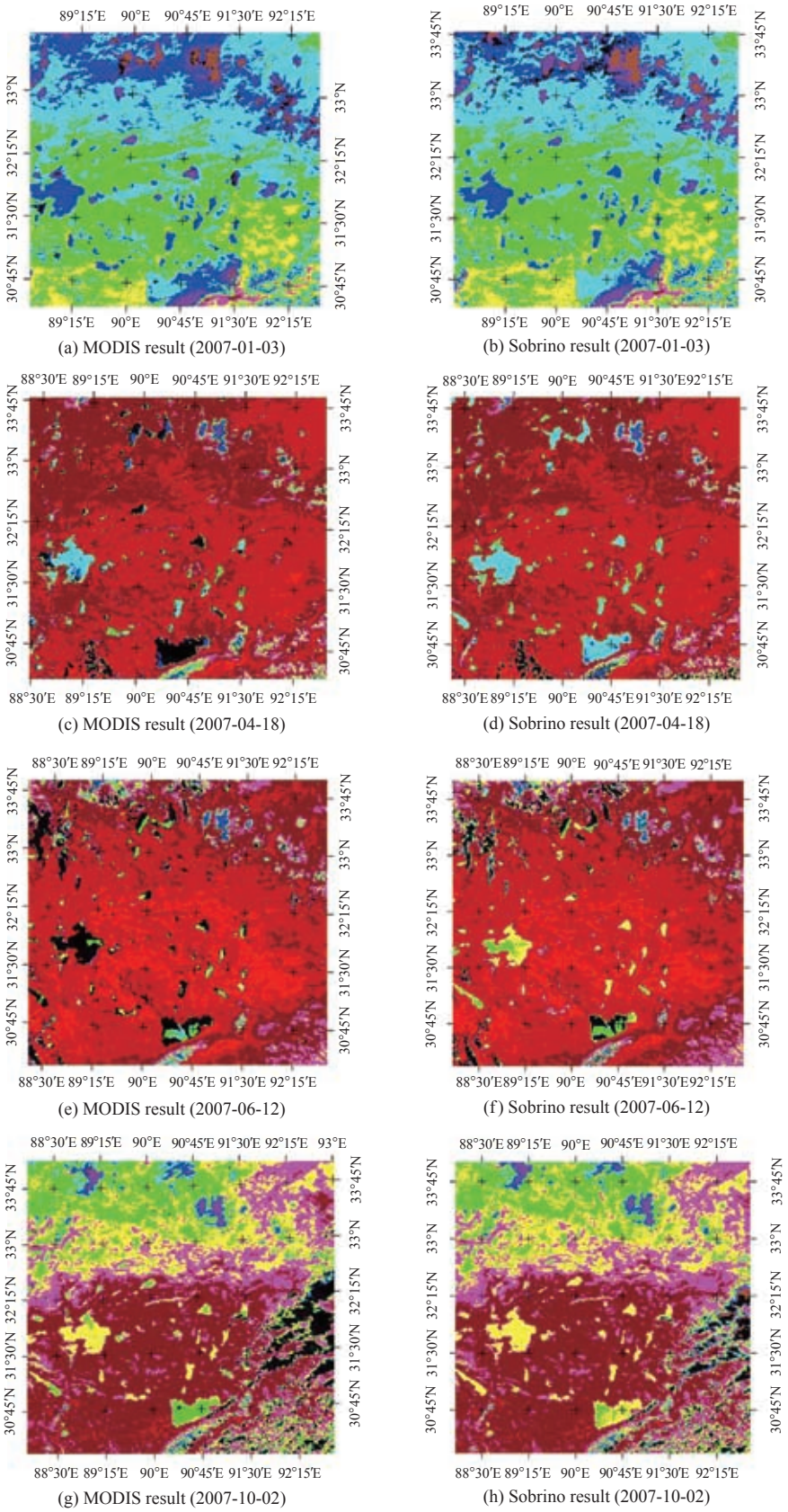

Fig. 4 Spatial distribution of MODIS product (Left) and LST RESULT (Right)

Table 3 Comparison of LST RESULT and MODIS product /K

Date		Max.	Difference	Min.	Difference	Average	Difference
2007.01.03	MODIS product	295.19	–0.52	256.57	–0.63	278.53	–0.43
	LST RESULT	295.71		257.20		278.96	
2007.04.18	MODIS product	318.65	0.31	268.90	0.35	302.68	0.20
	LST RESULT	318.34		268.55		302.48	
2007.06.13	MODIS product	322.55	–1.32	269.98	0.55	305.82	0.79
	LST RESULT	323.87		269.43		305.03	
2007.10.02	MODIS product	308.26	–0.73	264.75	13.02	291.78	0.05
	LST RESULT	308.99		251.73		291.73	

4.3 Validation with observation data

LST observation data from CAMP/Tibet sites were used to validate with LST RESULT from the same latitude and longitude. We could find from Table 4 that the absolute difference in Amdo site on January 3rd was –7.07 K. After analyzing with image and observation data, it could be caused by the dramatic changes of the observational data during the satellite passing time. Wu and Ma (2010) pointed out that upward long-wave radiation shows significant diurnal variation on Tibetan Plateau and the upward long-wave radiation usually reaches its maximum value between 14:00 (BJT) and 15:00 in Naqu area. On January 3rd 2007, the observational data from half-an-hour long-wave radiation reached its maximum at 12:30, and then drastically reduced, which caused LST reduce by 10.2 K in half hour. Finally, the observation data showed two peaks on that day. Since the validation data would change a lot during the satellite transit time, the observational data from half-an-hour radiation couldn't reflect the true situation. Furthermore, it should affect the accuracy of the verification.

The average error E can be calculated according to Eq. (16).

Table 4 Verification of MODIS product and LST RESULT with observation data /K

		MODIS product	LST RESULT	observation	Diff 1	Diff 2
2007-01-03	BJ	283.78	283.86	283.90	–0.12	–0.04
	NPAM	281.54	283.28	286.00	–4.46	–2.72
	D105	276.52	277.25	278.54	–2.02	–1.29
	Amdo	282.54	282.44	289.51	–6.97	–7.07
2007-04-18	BJ	308.44	309.58	311.11	–2.67	–1.53
	NPAM	307.84	306.82	306.14	1.70	0.68
	D105	304.10	304.73	No data		
	Amdo	310.86	310.56	No data		
2007-06-12	BJ	314.18	315.04	319.55	–5.37	–4.51
	NPAM	312.16	311.05	308.09	4.07	2.96
	D105	304.44	307.06	No data		
	Amdo	318.50	316.84	No data		
2007-10-02	BJ	Cloud	Cloud	No data		
	NPAM	297.66	295.79	295.74	1.92	0.05
	D105	289.00	289.23	288.78	0.22	0.45
	Amdo	300.80	299.88	299.76	1.04	0.12
E (Amdo, January 3rd, excluded)					2.359	1.435

Notes: Diff1 is difference between MODIS product and observation data; Diff2 is difference between LST RESULT and observation data; No data means data lost; cloud means cloud-covered pixel

$$E = \sum_{i=1}^{n} \frac{|T_{\text{Modis}i} - T_{\text{Site}i}|}{n} \tag{16}$$

where $T_{\text{Modis}i}$ is LST RESULT; $T_{\text{Site}i}$ is observation data; n is total number of data.

Fig. 5 shows the scatter graph of MODIS product, LST RESULT and observation data. In total, the average difference E between MODIS product and observation data (January 3rd 2007 Amdo site excluded) is 2.359 K while the E between LST RESULT and MODIS product was only 1.435 K.

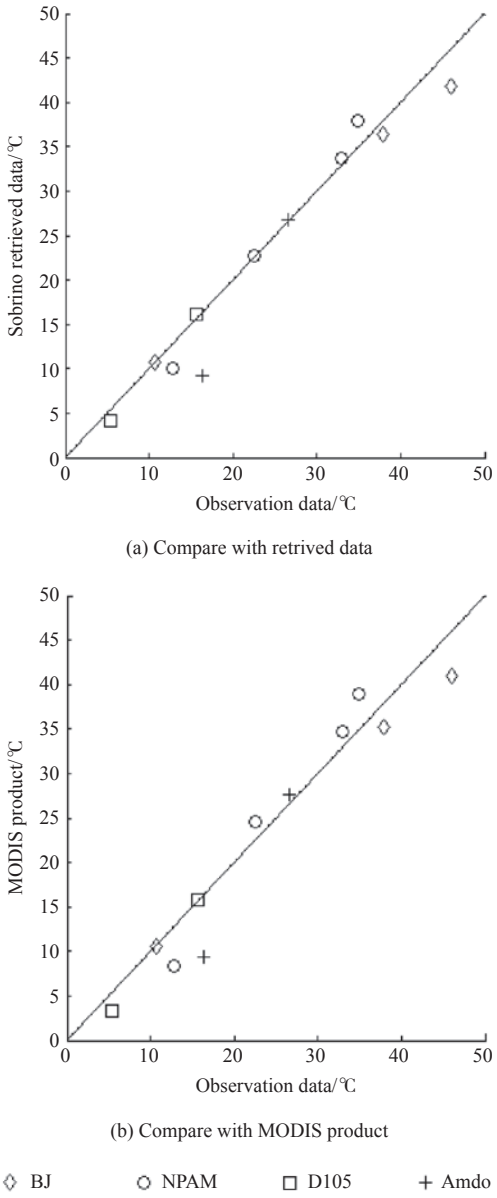

(a) Compare with retrived data

(b) Compare with MODIS product

Fig. 5 Scatter graphs of LST

5 CONCLUSIONS

Using the SWAs developed by Sobrino, with land surface classification (land, water and snow & ice) and sufficient and simple cloud-detect process, four land surface temperature images were retrieved for clear sky with EOS/MODIS in Naqu area over TP, including January, April, June and October in 2007. After that the derived LST was compared with the MODIS daily land surface temperature product and in-situ data from the Coordinated Enhanced Observing Period (CEOP) Asia-Australia Monsoon Project (CAMP)on the Tibetan Plateau (CAMP/Tibet). The conclusions are as below.

(1) Adding a simple cloud detection process based on simple land surface classification the improved Sobrino SWAs not only make the inversion algorithm more perfect, but also can be applied to special underlying surface such as snow & ice or water on TP.

(2) A simple validation of atmospheric WVC of Kaufman method and Sobrino method was carried out using the two days data of JICA project. In the end, Kaufman method can reflect the changes of atmospheric columnar WVC better and it was added to Sobrino SWAs for calculating LST.

(3) The LST result showed good agreement with MODIS product and observation data on the four days. Water, snow and other surfaces show good spatial distribution of LST. The four images can also simply reflect the seasonal variation and spatial variation of LST changing from south to north. In total, the LST inversion method is feasible.

(4) The average error between LST RESULT and observation data under cloud-free surface is only 1.435 K excluded abnormal data. Considering the scale difference between the inversion result and the ground observation data and the error between satellite transit time and instrument collection time, the error mentioned above is acceptable.

(5) The improved Sobrino LST inversion method only relies on original remote sensing data without other surface parameters and meteorological parameters. The inversion algorithm is reliable and the inversion result is consistent with the surface condition. It will be helpful for us to understand TP.

Discussion:

(1) Even if the cloud detection method is added, in this paper, it is still simplified to accurate interpretation for the pixels at the edge of the cloud. NDSI and thermal infrared brightness temperature difference can be helpful to be used as cloud-detection tests in improving cloud-detection process.

(2) Although more reasonable WVC calculation method was used, Sobrino, et al. (2003) concluded with numerical test simulation that atmospheric WVC has very small effect on final LST result.

(3) Ground observation LST data can only represent the small scale characteristic of temperature around the station. while MODIS inversion LST RESULT can represent 1 km scale. And the error should be caused by the scale difference of the instruments. Implementation of a more ideal LST experiment and using more appropriate method of data assimilation will improve our understanding with the LST inversion result.

REFERENCES

Becker F and Li Z L. 1990. Towards a local split window method over land surfaces. International Journal of Remote Sensing, 11(3): 369–393 [DOI: 10.1080/01431169008955028]

Carlson T N and Ripley D A. 1997. On the relation between NDVI, fractional vegetation cover, and leaf area index. Remote Sensing of Environment, 62(3): 241–252 [DOI: 10.1016/S0034-4257(97)00104-1]

Chen X L, Ma Y M, Li M S, Ma W Q and Wang H. 2008. Analyses on near surface layer atmospheric characteristics and soil features in northern Tibetan plateau. Plateau Meteorology, 27(5): 941–948

Coll C and Caselles V. 1997. A split-window algorithm for land surface temperature from advanced very high resolution radiometer data: validation and algorithm comparison. Journal of Geophysical Research, 102(D14): 16697–16713 [DOI: 10.1029/97JD00929]

Kaufman Y J and Gao B C. 1992. Remote sensing of water vapor in the

near IR from EOS/MODIS. Transactions on Geoscience and Remote Sensing, 30(5): 871–884 [DOI: 10.1109/36.175321]

Kerr Y H, Lagouarde J P and Imbernon J. 1992. Accurate land surface temperature retrieval from AVHRR data with use of an improved split window algorithm. Remote Sensing of Environment, 41(2/3): 197–209 [DOI: 10.1016/0034-4257(92)90078-X]

Li J. 2005. A Study of Land Surface Temperature Retrieval for the Region of Changbai Mountain of China. Changchun: Jilin University: 45

Liu Y J and Yang Z D. 2001. MODIS Remote Sensing Information Processing Principles and Algorithms. Beijing: Science Press

Ma W Q, Ma Y M, Li M S, Su Z and Wang J M. 2005. Seasonal variation on land surface energy budget and energy balance components in the Northern Tibetan Plateau. Journal of Glaciology and Geocryology, 27(5): 673–679

Ma Y M, Liu D S, Su Z B, Li Z L, Menenti M and Wang J M. 2004. Land surface variables and vegetation variables estimated from satellite remote sensing over inhomogeneous land surface of the northern Tibetan Plateau. Chinese Journal of Atmospheric Sciences, 28(1): 23–31

Ma Y M, Tsukaoto O, Ishikawa H, Su Z B, Menenti M, Wang J M and Wen J. 2002. Determination of regional land surface heat flux densities over heterogeneous landscape of HEIFE integrating satellite remote sensing with field observations. Journal of the Meteorological Society of Japan, 80(3): 485–501

Ma Y M, Yao T D, Wang J M, Hu Z Y, Ishikawa H, Ma W Q, Menenti M and Su Z B. 2006. The study on the land surface heat fluxes over heterogeneous landscape of the Tibetan Plateau. Advances in Earth Sciences, 21(12): 1215–1223

Mao K, Qin Z, Shi J and Gong P. 2005. A practical split window algorithm for retrieving land surface temperature from MODIS data. International Journal of Remote Sensing, 26(15): 3181–3204 [DOI: 10.1080/01431160500044713]

Price J C. 1984. Land surface temperature measurements from the split window channels of the NOAA 7 Advanced Very High Resolution Radiameter. Journal of Geophysical Research, 89(D5): 7231–7237 [DOI: 10.1029/JD089iD05p07231]

Qiu J. 2008. The third pole. Nature, 454(24): 393–396

Qin Z H, Dall O G and Karnieli A. 2001. Derivation of split window algorithm and its sensitivity analysis for retrieving land surface temperature from NOAA-advanced very high resolution radiometer data. Journal of Geophysical Research, 106(D19): 22655–22670 [DOI: 10.1029/2000JD900452]

Saunders R W and Kriebel K T. 1988. An improved method for detecting clear sky and cloudy radiances from AVHRR data. International Journal of Remote Sensing, 9(1): 123–150 [DOI: 10.1080/01431168808954841]

Sobrino J A and Caselles V. 1991. A methodology for obtaining the crop temperature from NOAA-9 AVHRR data. International Journal of Remote Sensing, 12(12): 2461–2475 [DOI: 10.1080/01431169108955280]

Sobrino J A, Li Z L, Stoll M P and Becker F. 1994. Improvements in the Split-Window Technique for Land Surface Temperature Determination. Transactions on Geoscience and Remote Sensing, 32(2): 243–253

Sobrino J A, Kharraz J E and Li Z L. 2003. Surface temperature and water vapour retrieval from MODIS data. International Journal of Remote Sensing, 24(24): 5161–5182 [DOI: 10.1080/0143116031000102502]

Sobrino J A and Raissouni N. 2000. Toward Remote Sensing methods for land cover dynamic monitoring: application to Morocco. International Journal of Remote Sensing, 21(2): 353–366 [DOI: 10.1080/014311600210876]

Wan Z and Li Z. 1997. A physics-based algorithm for retrieving land-surface emissivity and temperature from EOS/MODIS data. Transactions on Geoscience and Remote Sensing, 35(4): 980–996 [DOI: 10.1109/36.602541]

Wan Z, Zhang Y, Zhang Q and Li Z L. 2004. Quality assessment and validation of the MODIS global land surface temperature. International Journal of Remote Sensing, 25(1): 261–274 [DOI: 10.1080/0143116031000116417]

Wang X, Zhang Q, Guo N and Cai D H. 2007. Method for discriminating snow in Qilian Mountain region based on MODIS data. Arid Meteorology, 25(2): 29–34

Wu R S and Ma Y M. 2010. Comparative analyses on radiation characteristics in different areas over the Tibetan Plateau. Plateau Meteorology, 29(2): 251–259

Yang K, Koike T, Ishikawa H, Kim J, Li X, Liu H Z, Liu S M, Ma Y M and Wang J M. 2008. Turbulent flux transfer over bare-soil surfaces: characteristics and parameterization. Journal of Applied Meteorology and Climatology, 47(1): 276–290 [DOI: 10.1175/2007JAMC1547.1]

Yang H and Yang Z D. 2006. A modified land surface temperature split window retrieval algorithm and its applications over China. Global and Planetary Change, 52(1/4): 207–215 [DOI: 10.1016/j.gloplacha.2006.02.015]

Zhao Y S. 2003. Remote Sensing Application Analysis Theory and Method. Beijing: Science Press

Zhu W J. 2008. Retrieval land surface temperature from MODIS data base on single-channel method. Urban Geotechnical Investigation and Surveying, (5): 97–100

青藏高原那曲地区MODIS地表温度估算

王宾宾[1, 2, 3]，马耀明[1, 3]，马伟强[2, 3, 4]

1. 中国科学院 青藏高原研究所，北京 100085；
2. 中国科学院 研究生院，北京 100049；
3. 中国科学院 青藏高原环境变化与地表过程重点实验室，北京 100085；
4. 中国科学院 寒区旱区环境与工程研究所，甘肃 兰州 730000

摘 要：地表温度是区域和全球尺度陆面过程研究中的一个关键参数，利用遥感卫星资料反演得到的地表温度数据在气象、水文和生态领域研究中有重要作用。本文基于改进后的针对MODIS数据的分裂窗口算法，对MODIS L1B卫星数据进行实用而简便的云检测处理，并根据青藏高原陆地、水体和冰雪等常见下垫面状况的遥感影像分类结果，反演得到了2007-01-03、04-18、06-12和10-02四日的无云下垫面地表温度。最后，将Sobrino结果在青藏高原那曲地区与MODIS日地表温度产品及CAMP/Tibet观测站地表温度数据进行了对比验证分析。结果表明，该方法得到的地表温度结果与MODIS数据产品具有较好的一致性,并且地表温度结果与地面观测数据(去除可疑点后)的平均误差仅为1.435 K。

关键词：青藏高原，MODIS，分裂窗口算法，云检测，地表温度

中图分类号：P423.7 **文献标志码：**A

引用格式：王宾宾，马耀明，马伟强．2012．青藏高原那曲地区MODIS地表温度估算．遥感学报，16(6): 1289–1309
Wang B B, Ma Y M and Ma W Q. 2012. Estimation of land surface temperature retrieved from EOS/MODIS in Naqu area over Tibetan Plateau. Journal of Remote Sensing, 16(6): 1289–1309

1 引 言

青藏高原是世界上平均海拔最高、面积最大、地形最为复杂的高原，被称为地球的“第三极(Qiu，2008)”。青藏高原由于其高大的地形特征而使该地区在地气相互作用过程，尤其是能量与水分循环过程中对亚洲季风、东亚大气环流及全球气候变化均有极大的影响，属于全球气候变化的敏感地区(马耀明 等，2004)。尽管针对青藏高原陆地、大气及其相互作用过程的研究已经进行了多次大规模的野外观测实验(陈学龙 等，2008)，包括“第一次青藏高原实验”，“第二次青藏高原大气科学实验”，“全球能量水循环之亚洲季风青藏高原试验研究(Gloabal Energy and Water Cycle Experiment(GEWEX) and the Asia Monsoon Experiment on the TP，GAME/Tibet)”和“全球协调加强观测计划之亚澳季风之青藏高原试验研究(the Coordinated Enhanced Observing Period (CEOP) Asia-Australia Monsoon Project on the TP，CAMP/Tibet)”等，但由于青藏高原的严酷环境条件，使得以稀疏离散点为基础的青藏高原地表观测数据依旧匮乏。卫星遥感技术的应用将成为人们获取青藏高原地表参数的关键方法之一。

在地表与大气相互作用的研究中，地表温度是一个基本参数。地表温度被定义为地表的分子运动温度，它与卫星热红外传感器观测的辐射温度相区别(赵英时，2003)。地表温度是区域和全球尺度上地表物理过程研究的一个关键参数，它综合了所有地气相互作用和能量交换的结果(Zhu，2008)。常规的观测

收稿日期：2011-10-11；**修订日期：**2012-05-08

基金项目：中欧合作“龙计划”项目；全球变化国家重大科学研究计划(编号: 2010CB951701)；国家杰出青年科学基金(编号: 40825015)；中国科学院方向性项目 (编号: KZCX2-YW-QN309)

第一作者简介：王宾宾(1986—)，男，博士研究生，主要从事大气边界层和卫星遥感应用方面的研究工作。E-mail: wangbinbin@itpcas.ac.cn。

通信作者简介：马耀明(1964—)，男，研究员，主要从事大气边界层过程及卫星遥感应用研究。E-mail: ymma@itpcas.ac.cn。

方法仅能够获得单点或局地尺度的地表温度数据，而区域尺度甚至全球尺度的地表温度数据在环境研究和资源管理中的需求使得遥感卫星像元尺度的地表温度反演成为重要的研究课题(Yang和Yang，2006)。在过去的二十多年里，卫星遥感反演地表温度取得了巨大的进步，分裂窗口算法目前应用最为广泛。该算法基于辐射传输方程，利用10—13 μm大气窗口内两个相邻通道对大气吸收作用的不同，通过两个通道测量值的不同组合来剔除大气的影响，从而进行大气和地表比辐射率的订正(赵英时，2003)。Price(1984)首次利用，甚高分辨率辐射仪(Advanced Very High Resolution Radiometer，AVHRR)传感器两个热红外通道数据(4、5通道)，将海面温度遥感反演的分裂窗口算法应用到农田地区的温度反演中。随后，Becker和 Li(1990)，Sobrino和Caselles(1991)，Kerr等人(1992)，Sobrino等人(1994)，Coll和Caselles(1997)，Sobrino和Raissouni(2000)，Ma等人(2002)，Sobrino等人(2003)以及Mao等人(2005)分别致力于分裂窗口算法反演地表温度的研究中。其中，Sobrino地表温度反演方法是分裂窗口算法中发展历时较长、体系结构较为完善、反演操作流程较为简单的一种算法。

地球观测系统卫星EOS是美国地球观测系统计划中一系列卫星的简称。第一颗EOS的上午轨道卫星TERRA于1999-12-18日发射升空，其携带的最主要仪器是中分辨率成像光谱仪MODIS。MODIS数据覆盖范围大，它拥有36个光谱波段，大大提高了光谱分辨率并增强了对地球复杂系统的观测能力和对地表类型的识别能力(刘玉洁和杨忠东，2001)。本文利用MODIS L1B数据基于Sobrino地表温度反演方法，并对其进行适当改进，将其应用于青藏高原地区。最终选择青藏高原那曲地区地表温度反演结果与MODIS地表温度产品进行了验证并与实测的站点地表温度数据进行对比分析，最后分析讨论了该方法反演得到的高原那曲地区地表温度反演结果的精度。

2 数 据

2.1 MODIS原始数据

本文使用的MODIS L1B数据是2007年1月3日、4月18日、6月12日及10月2日HDF格式的MOD021-KM-Level 1B Calibrated Radiance-1km Terra卫星数据(所选4日影像高原整体的天空云覆盖面积较小，便于地表站点观测数据的验证)[1]。该数据已经过仪器标定，但没有经过大气校正。该数据需通过辐射定标公式将数据原始DN值转换为辐射亮度。定标公式为$L_i=scales_i\times(count_i-offset_i)$，式中的$scales_i$、$offset_i$为相应$i$通道的比例系数和偏移量，$count_i$是通道$i$的数字记录值(DN值)，$L_i$是定标后的辐射亮度。

2.2 MODIS地表温度产品

本文利用NASA数据服务网站[2]提供的全球每日1 km分辨率SIN投影坐标网格产品，等级为3的HDF格式的MODIS-Terra地表温度和比辐射率为v5版本的产品(MODIS/ Terra Land Surface Temperature/ Emissivity Daily L3 Global 1km SIN Grid v005)进行反演结果的初步验证。该套产品采用了基于物理的白天/黑夜地表温度反演方法(Wan和Li，1997)。地表温度产品在较大范围的下垫面状况和较大范围的大气水汽状况下均做了验证，其精度小于1 K(Wan 等，2004)。数据产品在验证前需通过MODIS重采样工具MRT(MODIS Reprojection Tools)进行投影坐标转换和影像镶嵌。

2.3 站点验证数据

本文所用到的常规气象站验证资料来自于CAMP/Tibet试验气象观测资料(站点包括：NPAM、BJ、D105和 Amdo)。GAME/Tibet(1996年—2000年)以研究青藏高原地表与大气之间能量交换作为首要科学任务，在藏北那曲地区一个150 km × 200 km的区域内包括高原草甸、高原湖泊和荒漠化草原等不同下垫面上设置了大量的观测站点。GAME/Tibet项目结束后，即刻加入全球能量和水循环实验GEWEX与气候变化和预测CLIVAR(the Climate Variability and Predictability)两个大型国际计划联合组织的“全球协调加强观测计划”，进行CAMP/Tibet研究，原有试验站和新加入的试验站绝大部分仪器仍在连续观测，取得了十分宝贵的资料(Ma 等，2006)。

4个观测站点的基本情况如下(Ma 等，2002；马伟强 等，2005)：NPAM站(91°72′E，31°93′N)，试验场地面平坦，东边约5 km、西边约30 km、南北约10 km处分布着相对高度约100—200 m的山丘，地面为高原草甸覆盖。BJ站(91°54′E ，31° 22′N)试

[1] [2010-08-15] https://ladsweb.nascom.nasa.gov/index.htm
[2] [2010-09-15] https://wist.echo.nasa.gov/api/

验场地四周开阔，地面为高原草甸覆盖。D105站(91°94′E，33°06′N)，试验场地面平坦，视野开阔，东边约20 km处有山丘，地面为高原稀疏草甸。Amdo(91°37′E，32°14′N)站下垫面相对平坦，场地四周开阔，地面为高原稀疏草甸。选取的观测场地的地形和下垫面特征使得气象观测资料可以代表站点及周边较大区域范围的平均状况。4个站点均安装有地表辐射温度计HR1-FL、两个埋深0 cm的Pt/100温度计以及四向辐射仪器。D105站、NPAM站和Amdo站的向上和向下短波及长波辐射表均为Kipp&Zonenn Pyramometer CM21，探头高度分别为1.58 m和1.28 m，NPAM和D105的辐射仪器采样时间为1 h，Amdo站的采样时间为30分钟；BJ站测量向上和向下的长波辐射和短波辐射分别为Eppley PIR和EKO MS-801，仪器架设高度为1.5 m，采样时间为10 min。

利用NPAM、BJ、D105和Amdo 4个站点的向上长波辐射和向下长波辐射数据，我们可以推算各站点地表皮肤温度，最终综合各种观测仪器地表温度数据剔除有较大偏差的数据，并对观测数据依据时间进行了线性插值以便与卫星过境时刻相对应，最终获取最可靠的地表温度验证数据。长波辐射推算地表温度的计算方法如式(1)所示(Yang 等，2008)：

$$R_{\mathrm{lw}}^{\uparrow}=(1-\varepsilon_s)R_{\mathrm{lw}}^{\downarrow}+\varepsilon_s\sigma T_{\mathrm{g}}^{4} \tag{1}$$

式中，T_{g}为地表皮肤温度，$R_{\mathrm{lw}}^{\uparrow}$是长波向上辐射，$R_{\mathrm{lw}}^{\downarrow}$是长波向下辐射，$\sigma=5.67\times10^{-8}\mathrm{W\cdot m^{-2}\,K^{-4}}$是斯蒂芬-波尔兹曼常数。$\varepsilon_s$是地表比辐射率，考虑到观测场地以高原草甸为主，结合Yang等人(2008)的分析，可近似取0.9800。

3 MODIS地表温度估算方法

分裂窗口算法估算地表温度的关键是无云大气条件下地表比辐射率、大气水汽含量、遥感热红外通道亮度温度等参数的计算。遥感估算地表温度的整体流程如图1所示。

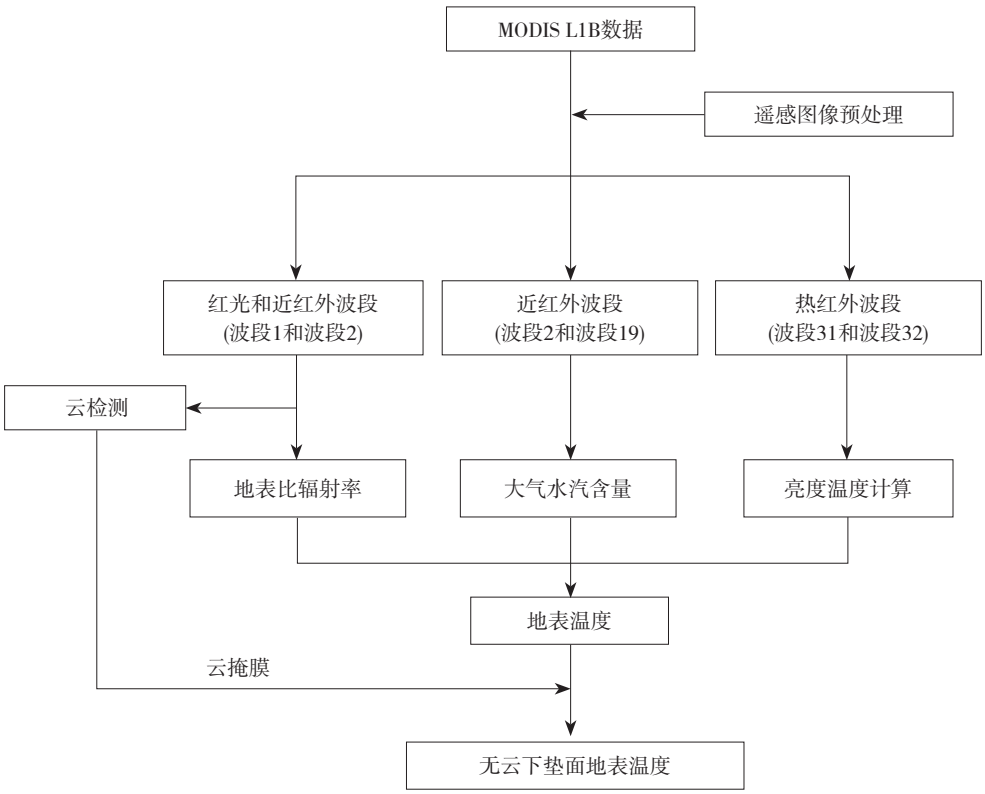

图1 MODIS地表温度估算流程

3.1 数据预处理

首先，我们对MODIS L1B卫星数据进行以下预处理：(1)通过从地理坐标定位的头文件中抽取经纬度值对原始数据进行地理坐标定位。(2)通过蝴蝶结现象去除来消除图像边缘像元重叠现象。(3)通过基于移植了MODTRAN4.0(MODerate spectral resolution

atmospheric TRANSsmittance algorithm and computer model 4.0，中光谱分辨率大气透过率算法与计算模型4.0)的辐射传输计算方法的FLAASH模块(Fast Line-of-sight Atmospheric Analysis of Spectral Hypercubes module)进行大气辐射校正以去除大气中水蒸气、二氧化碳、甲烷和臭氧以及大气分子和气溶胶散射对地物反射率的影响，大气辐射校正结果用于归一化植被指数(NDVI)以及云检测过程的阈值计算。以上处理过程我们通过ENVI+IDL的遥感图像处理软件系统来完成。

3.2 云检测

分裂窗口算法的理论基础是局地热力学平衡无云大气条件下的热辐射传输方程。因此，在对遥感影像进行地表温度反演之前，我们需要对MODIS数据进行云检测。Saunders和Kriebel(1988)提出了针对AVHRR 影像的无云像元识别方法。我们利用其提出的无云像元判读识别原理，通过遥感影像人工判读识别的方法，实现对MODIS遥感影像无云像元的提取，并最终计算无云像元的地表温度。(1)第一个检测条件是红外阈值检测：由于云在12 μm波段范围内有更大的光学厚度，因此，若12 μm的亮度温度低于某一阈值($T_{32}<280$ K)，我们认为该像元可能被云覆盖或为冰雪区域；(2)第二个检测条件我们利用近红外反射率和可见光反射率的比值Q。无云大气条件下的水面，由分子和气溶胶散射效应的短波后向散射引起可见光波段的反射率是近红外波段的两倍，因此，Q接近于0.5；在陆地表面(雪、冰除外)，可见光反射率要比近红外反射率小的多，因此，Q总是大于1；而在云团或冰雪表面，可见光波段反射率与近红外波段反射率相差不大，因此，Q接近于1。因此，我们用$a_1<\rho_{nir}/\rho_r<a_2$来表示可能被云覆盖区域或冰雪区域，其中$a_1$、$a_2$用人工判读的方式从图像中获得。(3)云像元与冰雪像元的区分：我们可利用云在短波红外波段(波段6)的反射率明显高于冰雪在短波红外波段的反射率的特性，利用$\rho_6>c$将冰雪像元排除，其中c根据图像确定。只有同时满足以上3个条件的像元我们才能将该像元判别为云。在云检测的过程中结合图像特征，我们可以将遥感卫星图像分类为陆地、水体、云和冰雪4种类型。

3.3 亮度温度计算

普朗克函数给出了黑体发射的光谱辐射在指定波长和温度下的形式如式(2)：

$$B_\lambda(T)=2hc^2\lambda^{-5}\times[\exp(hc/\lambda kT)-1]^{-1} \tag{2}$$

式中，$B_\lambda(T)$为黑体光谱辐射值，h为普朗克常数，c为光速，λ为波长，k为玻尔兹曼常数，T为热力学温度。因此，普朗克函数经过逆变换(Qin 等，2001)可得式(3)：

$$T=\frac{c_2}{\lambda\ln\left[\left(\frac{2c_1}{\lambda^5 B_\lambda(T)}+1\right)\right]} \tag{3}$$

式中，c_1=5.95522012×10^{-17} W·m^2，c_2=1.43876869×10^{-2} m·K，遥感卫星数据的通道辐射率值经过普朗克函数的逆变换可转换为通道的亮度温度。

3.4 地表比辐射率的计算

地表比辐射率不仅与地表物质的组成成分、表面状态及物理性质有关而且也取决于遥感器的波段区间选择(赵英时，2003)。地球表面的地表结构虽然复杂，但是从MODIS 1 km空间分辨率来看，青藏高原地表大体上可以看作由4种地表类型构成：植被、裸土、水体以及冰雪面。

Sobrino 等(2003)提出了NDVI阈值法对植被和裸土进行地表比辐射率的估计，光谱平均比辐射率ε和光谱差值比辐射率$\Delta\varepsilon$通过以下公式计算。

当地表为混合地表的混合像元(即0.2 < NDVI < 0.5)，如式(4)(5)所示：

$$\varepsilon=0.971+0.018P_v \tag{4}$$

$$\Delta\varepsilon=0.006(1-P_v) \tag{5}$$

当地表为完全植被覆盖的像元时(即NDVI≥0.5)，如式(6)(7)所示：

$$\varepsilon=0.985+d\varepsilon \tag{6}$$

$$\Delta\varepsilon=0 \tag{7}$$

当地表为裸地覆盖像元时(即NDVI≤0.5)，如式(8)(9)所示：

$$\varepsilon=0.9832-0.058\rho_1 \tag{8}$$

$$\Delta\varepsilon=0.0018-0.060\rho_1 \tag{9}$$

式(4)—(9)中，ρ_1和ρ_2是MODIS通道1和通道2的光谱反射率；$d\varepsilon$是自然表面的几何分布与内部反射效应而引起的比辐射率比例。本文$d\varepsilon$=0.005。NDVI如式(10)，P_v是像元的植被覆盖度(Carlson和Ripley，1997)，如式(11)：

$$\mathrm{NDVI}=\frac{\rho_2-\rho_1}{\rho_2+\rho_1} \tag{10}$$

$$P_v=\left(\frac{\mathrm{NDVI}-\mathrm{NDVI}_{\min}}{\mathrm{NDVI}_{\max}-\mathrm{NDVI}_{\min}}\right)^2 \tag{11}$$

在实际研究中，根据研究区域的地表类型特点确定NDVI_{max}和NDVI_{min}。如果有明显的裸土区，则取裸土区的平均NDVI值作为NDVI_{min}。如果有明显的植被完全覆盖区，则取植被完全覆盖区的平均NDVI值作为NDVI_{max}。本文结合遥感卫星图像在青藏高原那曲地区的整体状况取值：NDVI_{max}=0.55，NDVI_{min}=0.05。

青藏高原存在高原冰川和高原湖泊等特定下垫面状况。对于湖泊，由于水体结构单一，一般比辐射率为0.97—1.0。MODIS 31和32波段的比辐射率分别取值为0.992、0.988(Mao 等，2005)。所以水体下垫面两波段的平均比辐射率ε为0.990，两波段差值比辐射率$\Delta\varepsilon$为0.004。对于冰雪表面李健(2005)指出：MODIS 31、32波段的比辐射率可分别取值为0.988和0.977，所以冰雪下垫面两波段的平均比辐射率ε为0.9825，两波段的差值比辐射率$\Delta\varepsilon$为0.011。Sobrino等(2003)指出平均比辐射率ε大小0.005的不确定性误差所造成的地表温度结果的不确定性大小为0.64 K。因此，使用前述比辐射率经验值所造成的地表温度估算结果的不确定性较小。

3.5 Kaufman大气水汽的估算

Kaufman和Gao(1992)在实验中发现通过表观反射率比率方法来反演大气水汽是可行的。

$$\tau_i=\rho_i/\rho_2 \tag{12}$$

式中，ρ_i (i=17，18，19)和ρ_2分别代表波段i和波段2表观反射率，τ_i代表i通道的透过率。然后利用Kaufman和Gao得出的大气水汽含量W与通道透过率τ_i (19/2)的拟合公式如式(13)所示：

$$\tau_i(19/2)=\exp(\alpha-\beta\sqrt{w}) \tag{13}$$

式中，通道透过率与大气水汽的相关系数为0.999，对于复杂地表，α=0.02，β=0.65，因此:

$$W=\left(\frac{0.02-\ln\tau_i}{0.65}\right)^2 \tag{14}$$

通过以上公式可以计算MODIS影像每个像元的地表平均比辐射率、地表差值比辐射率、31和32通道亮度温度及大气柱水汽含量。由此，借助于Sobrino经验公式(15)，便可以计算地表温度。

$$T_{sfc}=T_{31}+1.02+1.79\times(T_{31}-T_{32})+1.20\times(T_{31}-T_{32})^2+(34.83-0.68W)(1-\varepsilon)+(-73.27-5.19W)\times\Delta\varepsilon \tag{15}$$

式中，T_{31}、T_{32}是MODIS第31和第32通道的亮度温度，W是大气柱水汽含量，ε为平均地表比辐射率，$\Delta\varepsilon$为地表差值比辐射率，T_{sfc}为反演地表温度结果。

4 结果分析及精度评价

4.1 大气水汽含量估算方法的选取

大气水汽计算方法分别可利用Sobrino等人(2003)提出的MODIS数据的通道辐射值比值法(Sobrino方法)或通道表观反射率比值法(Kaufman方法)进行大气水汽的估算。Sobrino方法与Kaufman方法都采用大气窗口通道(MODIS第2、5波段)与大气水汽吸收通道(MODIS第17、18和19波段)的比值来近似描述大气水汽吸收通道的透过率，然后通过模型模拟大气水汽含量与大气透过率之间的关系来推算大气水汽含量。Sobrino等人(2003)使用MODTRAN模型来模拟辐射值比值与大气水汽含量的关系，而Kaufman等人(1992)使用的是LOWTRAN模型来模拟表观反射率比值与大气水汽含量的关系。两种大气水汽的计算方法都比较简单，可操作性也都较强。

我们利用日本国际合作机构JICA(Japan International Co-operation Agency)项目2008年GPS大气水汽站点观测资料结合MODIS大气水汽卫星数据产品，同时选取青藏高原及其周边区域观测站点2008年1月6日与1月7日的MODIS L1B卫星影像对两种方法进行了验证与评估。对比结果如表1、表2及图2所示。

表1 2008-01-06观测站点GPS实测值与MODIS产品、Sobrino方法及Kaufman方法的大气水汽含量的对比 /cm

站名	经度/(°E)	纬度/(°N)	MODIS产品	Sobrino方法	Kaufman方法	GPS实测值
改则	84.06221	32.30626	0.397	0.874	0.326	无值
甘孜	99.99755	31.61966	0.253	0.882	0.319	0.3074
林芝	94.36041	29.64812	0.548	0.484	0.748	无值
隆子	92.46006	28.41416	0.189	1.424	0.147	0.1415
那曲	92.06118	31.47977	0.236	1.422	0.147	0.2073
申扎	88.70490	30.93161	0.212	1.40	0.152	无值
昌都	97.17428	31.14696	0.248	0.996	0.270	无值
德钦	98.90737	28.48851	0.187	0.932	0.296	0.2462
丁青	95.59356	31.41513	0.295	0.966	0.282	0.1734
定日	87.12039	28.65461	0.307	1.199	0.201	无值

表2 2008-01-07观测站点GPS实测值与MODIS产品、Sobrino方法及Kaufman方法的大气水汽含量的对比 /cm

站名	经度/(°E)	纬度/(°N)	MODIS产品	Sobrino方法	Kaufman方法	GPS实测值
丽江	100.21865	26.84876	0.602	0.467	0.750	0.799
大理	100.17593	25.70729	0.727	0.449	1.067	0.533
甘孜	99.99755	31.61966	0.279	0.939	0.293	无值
昆明	102.65295	25.00769	0.401	0.515	0.678	0.53
林芝	94.36041	29.64812	0.588	0.446	0.949	0.74
理塘	100.27077	29.99468	0.333	1.143	0.219	0.444
隆子	92.46006	28.41416	0.420	0.612	0.526	0.342
腾冲	98.49748	25.01855	0.782	0.447	1.056	0.919
威宁	104.28078	26.86327	0.388	0.642	0.481	无值
西昌	102.26766	27.90411	0.881	0.493	1.369	0.776
昌都	97.17428	31.14696	0.291	1.021	0.261	无值
德钦	98.90737	28.48851	0.432	0.745	0.4	0.514
丁青	95.59356	31.41513	0.396	0.769	0.387	无值

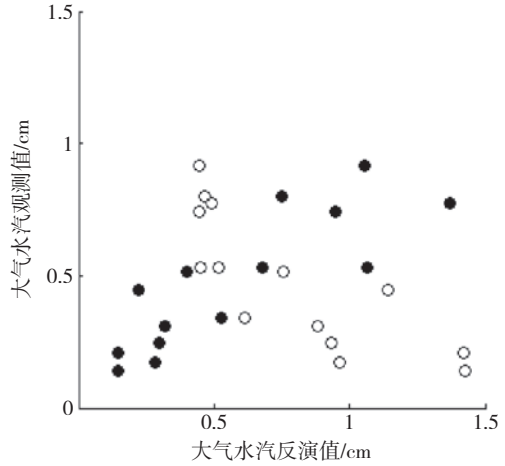

(a) 与大气水汽观测值的对比

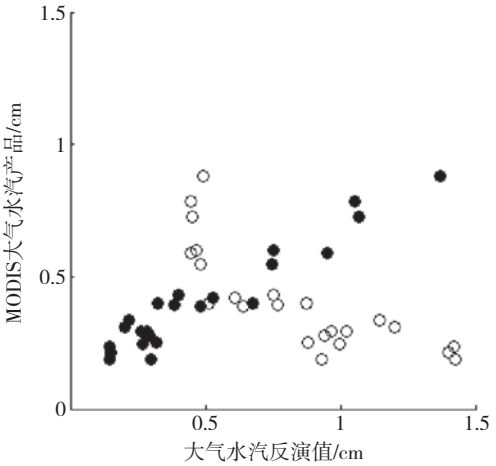

(b) 与MODIS产品的对比

○ Sobrino ● Kaufman

图2 反演大气水汽散点图

从大气水汽含量的反演结果与MODIS产品及GPS实测值的大气水汽对比散点图(图2)我们明显发现：Sobrino方法得到的结果(空心圆)与GPS大气水汽实测结果之间几乎毫无规律，而Kaufman方法(实心圆)得到的结果则整体较为理想；并且Kaufman方法得到的结果与MODIS产品结果也较为一致。因此，Kaufman方法得到的大气水汽结果在青藏高原及其周边区域较为可信，在MODIS数据反演青藏高原地表温度的过程中我们选用Kaufman方法来替代原始算法中的Sobrino大气水汽估算方法。

4.2 卫星遥感反演结果与MODIS产品的验证

图3分别为那曲地区遥感卫星图像Sobrino地表温度反演结果直方图与MODIS产品地表温度直方图。图4为那曲地区两者地表温度彩色空间分布图。图3所示Sobrino地表温度结果与MODIS产品地表温度直方图的分布具有较一致的特征。图4地表温度空间彩色分布图也同样显示出较一致的空间分布特征，从4幅影像的温度反演结果我们可以看到那曲地区从南向北温度随纬度增大而逐渐降低。在地表温度彩色空间分布图中，纳木错湖区域(4月18日)和色林错湖区域(6月12日)分别在MODIS产品中被检测为云覆盖区域。由于冰雪在0.555 μm(MODIS波段4，绿波段)反射率很高，而在1.64 μm(MODIS波段6，短波红外)的反射率很低；而云在绿波段和短波红外波段的反射率都较高，因此，我们可以利用归一化差值积雪指数(NDSI)来区分云和雪(王兴 等，2007)。经积雪指数验证：4月份影像中纳木错湖区域积雪指数较高，同时，可见光波段反射率较高而短波红外波段的反射率很低，依此判断：MODIS产品将纳木错湖面区域识别为云的结果很可能是错误的。纳木错湖区域在本文中被认为是冰或雪覆盖，这也符合4月份的天气状况；6月份遥感影像中色林错湖区域积雪指数很低，而短波红外波段的反射率也同样不高，因此，色林错湖区域云覆盖状况需更多辅助资料来判断。

表3是4幅影像Sobrino地表温度反演结果与MODIS产品最大值、最小值及平均值的对比(其中的最大值、最小值以统计结果中超过10个像元的温度作为边界最值)。同时，4幅影像的温度平均值也能够简单反映4个月份地表温度的季节变化特征。从表3我们可以看到，裁剪区域4幅影像的平均值差值都小于1 K，最大的平均值差值仅为0.79 K。2007-10-02其最

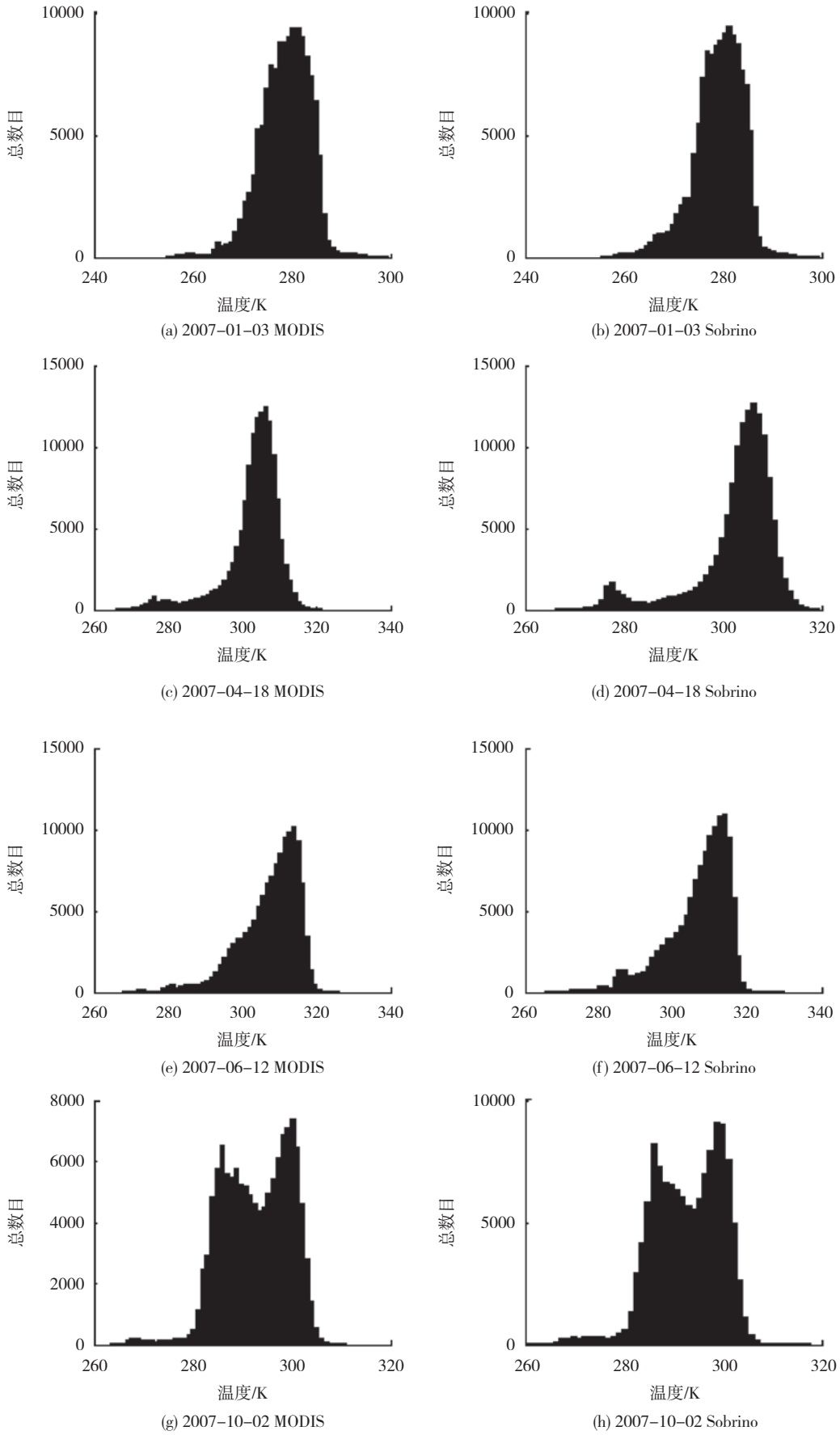

(a) 2007-01-03 MODIS (b) 2007-01-03 Sobrino

(c) 2007-04-18 MODIS (d) 2007-04-18 Sobrino

(e) 2007-06-12 MODIS (f) 2007-06-12 Sobrino

(g) 2007-10-02 MODIS (h) 2007-10-02 Sobrino

图3 MODIS产品温度和Sobrino地表温度反演结果分布直方图

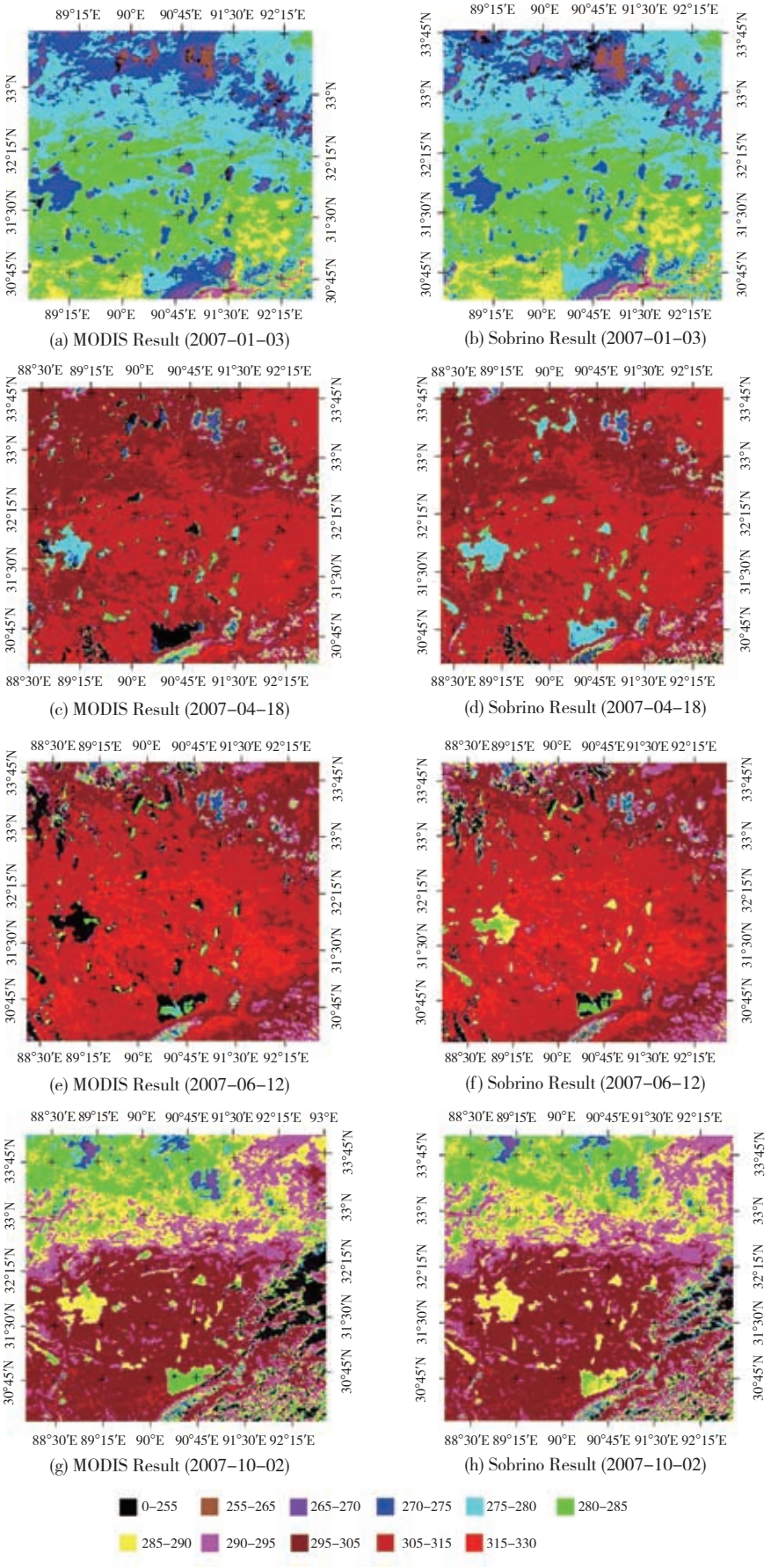

图4 MODIS产品和Sobrino地表温度反演结果彩色空间分布图

小值差值为13.02 K。这是由于本文所采用的云检测方法为3.2节所述简单阈值法，这些阈值的确定我们通过人眼判读识别的方法确定。而10月2日在那曲地区影像东南区域存在大量的云团，云检测方法的不完善造成云团边缘云像元的漏判，因此导致统计结果中最小值(代表云团)的偏低。

2007-06-13 MODIS产品和本文结果的最大值差值为–1.32 K，反演方法所产生的地表温度结果较高。在地表温度统计分析中，Sobrino地表温度结果中发现一些超过最大值323.87 K的少于10个像元的温度高值，它们在MODIS第31和32波段的亮度温度差值都较大。而由式(15)可知，Sobrino地表温度的反演结果受通道31和通道32的亮度温度差值的影响较大，两通道的亮度温度差值越大，地表温度反演结果也越高。因此，在云检测流程中，需要将亮度温度差值作为像元受云团污染的判定条件。

表3 遥感反演地表温度结果与MODIS产品的对比 /K

日期		最大值	差值	最小值	差值	平均值	差值
2007–01–03	MODIS产品	295.19	–0.52	256.57	–0.63	278.53	–0.43
	Sobrino结果	295.71		257.20		278.96	
2007–04–18	MODIS产品	318.65	0.31	268.90	0.35	302.68	0.20
	Sobrino结果	318.34		268.55		302.48	
2007–06–13	MODIS产品	322.55	–1.32	269.98	0.55	305.82	0.79
	Sobrino结果	323.87		269.43		305.03	
2007–10–02	MODIS产品	308.26	–0.73	264.75	13.02	291.78	0.05
	Sobrino结果	308.99		251.73		291.73	

4.3 卫星遥感反演结果与地面站点资料的验证

最后，利用CAMP/Tibet观测站的地表温度数据与该经纬度像元反演的地表温度结果进行了对比。从表4给出的结果可以看到：1月3日Amdo站的绝对误差值较大为–7.07 K。分析遥感数据及站点观测数据发现：这可能是由站点观测数据在卫星观测时刻剧烈变化引起的观测数据不确定性造成的。Wu和Ma(2010)研究指出，青藏高原地区向上长波辐射有明显的日变化特征，那曲地区向上长波辐射值在午后14时—15时(BJT)达到最大值。1月3日，该站点的半小时长波辐射观测数据在12：30达到最大值，然后急剧降低，引起长波推算的地表温度结果在13：00与13：30的半个小时时间段内降低了10.2 K，最终使地表温度数据在该日呈现双峰特征。因此，地表温度验证数据在卫星过境时间段内的强烈的变化势必会造成半小时站点地表观测结果不能准确反映卫星过境时刻地表温度的真实状况，从而影响地表温度的验证精度。将站点实测数据与站点所在像元的卫星遥感反演结果按式(16)计算其平均误差E：

表4 MODIS产品、地表温度反演结果及观测资料地表温度的验证 /K

		MODIS 产品	Sobrino LST结果	站点观测	Diff1	Diff2
2007–01–03	BJ	283.78	283.86	283.90	–0.12	–0.04
	NPAM	281.54	283.28	286.00	–4.46	–2.72
	D105	276.52	277.25	278.54	–2.02	–1.29
	Amdo	282.54	282.44	289.51	–6.97	–7.07
2007–04–18	BJ	308.44	309.58	311.11	–2.67	–1.53
	NPAM	307.84	306.82	306.14	1.70	0.68
	D105	304.10	304.73	无值		
	Amdo	310.86	310.56	无值		
2007–06–12	BJ	314.18	315.04	319.55	–5.37	–4.51
	NPAM	312.16	311.05	308.09	4.07	2.96
	D105	304.44	307.06	无值		
	Amdo	318.50	316.84	无值		
2007–10–02	BJ	云	云	无值		
	NPAM	297.66	295.79	295.74	1.92	0.05
	D105	289.00	289.23	288.78	0.22	0.45
	Amdo	300.80	299.88	299.76	1.04	0.12
E (Amdo站 1月3日 除外)					2.359	1.435

注：Diff1指MODIS产品与观测资料的差值；Diff2指Sobrino结果与观测资料的差值；无值指观测资料缺失；云指像元被云覆盖

$$E=\sum_{i=1}^{n}\frac{|T_{\mathrm{Modis}i}-T_{\mathrm{Site}i}|}{n} \tag{16}$$

式中，$T_{\mathrm{Modis}i}$是MODIS数据遥感反演结果，$T_{\mathrm{Site}i}$是观测站点实测数据，n为数据个数。

图5为各站点MODIS产品、地表温度反演结果与实测值的散点图。从总体来看，MODIS产品与地面观测数据(2007-01-03 Amdo站的误差值除外)的平均误差为2.359 K，而改进后的地表温度反演方法得到的结果(2007-01-03 Amdo站的数据除外)与站点观测数据的平均误差值仅为1.435 K。

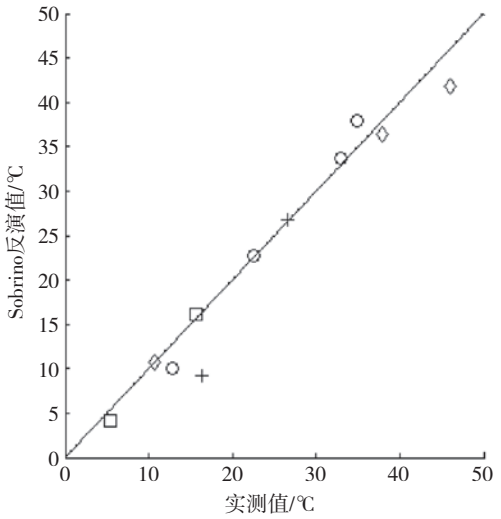

(a) 实测值与Sobrino反演结果

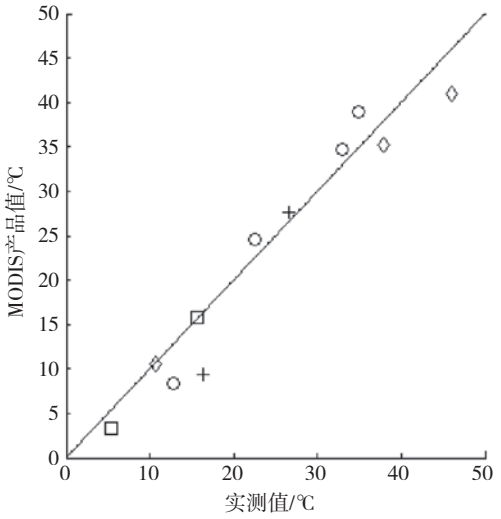

(b) 实测值与MODIS产品

◊ BJ ○ NPAM □ D105 + Amdo

图5 地表温度散点图

5 结 论

本文基于改进后的Sobrino于2003年提出的针对MODIS数据的分裂窗口算法，对MODIS L1B卫星数据进行实用而简便的云检测处理并最终反演得到了青藏高原那曲地区1月3日、4月18日、6月12日和10月2日共4日的无云下垫面地表温度，最后分别与MODIS每日的地表温度产品及CAMP/Tibet观测站的地表温度数据进行了对比验证分析，结论如下：

(1)添加简单云检测过程的基于地表简单分类的改进后的Sobrino分裂窗口算法不仅使地表温度的反演算法更加完善，而且使算法本身适用于带有冰雪、水体等特殊下垫面状况的高原。

(2)使用JICA项目两天的资料对大气水汽含量计算的Kaufman方法和Sobrino方法进行了简单的验证。Kaufman方法能更好的反映实际大气水汽含量的变化，因此，将Kaufman大气水汽计算方法应用于Sobrino分裂窗口算法计算地表温度的过程中。

(3)方法反演得到的4个日期的地表温度结果与MODIS数据产品以及地表观测数据显示出了较好的一致性。水体、冰雪表面及其他地面类型都显示了较好的温度空间分布特点。4幅影像也能够简单反映4个月份季节性的温度变化特征及由南向北地表温度降低的空间变化特征。因此，这种地表温度的反演方法是可行的。

(4)卫星遥感反演得到的无云下垫面地表温度数据与地面观测数据的平均误差为1.435 K(异常观测点除外)。考虑到MODIS卫星反演结果与地面观测数据的尺度差异以及卫星过境时刻与仪器采集时间分辨率引起的可能误差等，这种误差结果可以接受。

(5)这种改进后的地表温度反演算法不需要其他地表参数及其他气象参数的输入，而仅仅依赖原始遥感数据，实用性强；而且算法的反演结果与地表状况也较为吻合，反演结果也较为可信。它能够帮助我们加深对青藏高原的了解。

讨论及不足：(1)本文虽然添加了云检测过程，但由于检测方法过于简化，造成云团边缘云像元的漏判。归一化积雪指数和热红外通道亮度温度差值等更多云判读条件的使用将能够完善我们的云像元识别流程。(2)虽然采用了较为合理的大气水汽含量估算方法，但Sobrino等人(2003)对公式采用数值试验模拟指出：大气水汽含量W对于地表温度的计算结果影响较小。(3)地面站点观测数据仅代表站点周边小范围内的温度特征，而MODIS卫星图像的反演结果则代表1 km尺度的像元温度，仪器观测范围的差异必

然使两者之间存在一定的误差。实施更为理想的地表温度试验，采用更加合适的数据同化方法将能够进一步提高人们对遥感卫星地表温度估算结果的认识与理解。

参考文献(References)

Becker F and Li Z L. 1990. Towards a local split window method over land surfaces. International Journal of Remote Sensing, 11(3): 369–393 [DOI: 10.1080/01431169008955028]

Carlson T N and Ripley D A. 1997. On the relation between NDVI, fractional vegetation cover, and leaf area index. Remote Sensing of Environment, 62(3): 241–252 [DOI: 10.1016/S0034-4257(97)00104-1]

陈学龙, 马耀明, 李茂善, 马伟强, 王宏. 2008. 藏北地区近地层大气和土壤特征量分析. 高原气象, 27(5): 941–948

Coll C and Caselles V. 1997. A split-window algorithm for land surface temperature from advanced very high resolution radiometer data: validation and algorithm comparison. Journal of Geophysical Research, 102(D14): 16697–16713 [DOI: 10.1029/97JD00929]

Kaufman Y J and Gao B C. 1992. Remote sensing of water vapor in the near IR from EOS/MODIS. Transactions on Geoscience and Remote Sensing, 30(5): 871–884 [DOI: 10.1109/36.175321]

Kerr Y H, Lagouarde J P and Imbernon J. 1992. Accurate land surface temperature retrieval from AVHRR data with use of an improved split window algorithm. Remote Sensing of Environment, 41(2/3): 197–209 [DOI: 10.1016/0034-4257(92)90078-X]

李健. 2005. 长白山地区地表温度研究. 长春: 吉林大学硕士: 45

刘玉洁, 杨忠东. 2001. MODIS遥感信息处理原理与算法. 北京: 科学出版社

马伟强, 马耀明, 李茂善, Su Z, 王介民. 2005. 藏北高原地区地表辐射出支和能量平衡的季节变化. 冰川冻土, 27(5): 673–679

马耀明, 刘东升, 苏中波, 李兆良, Menenti M, 王介民. 2004. 卫星遥感藏北高原非均匀陆表地表特征参数和植被参数. 大气科学, 28(1): 23–31

Ma Y M, Tsukaoto O, Ishikawa H, Su Z B, Menenti M, Wang J M and Wen J. 2002. Determination of regional land surface heat flux densities over heterogeneous landscape of HEIFE integrating satellite remote sensing with field observations. Journal of the Meteorological Society of Japan, 80(3): 485–501

马耀明, 姚檀栋, 王介民, 胡泽勇, 石川裕彦, 马伟强, Menenti M, 苏中波. 2006. 青藏高原复杂地表能量通量研究. 地球科学进展, 21(12): 1215–1223

Mao K, Qin Z, Shi J and Gong P. 2005. A practical split window algorithm for retrieving land surface temperature from MODIS data. International Journal of Remote Sensing, 26(15): 3181–3204 [DOI: 10.1080/01431160500044713]

Price J C. 1984. Land surface temperature measurements from the split window channels of the NOAA 7 Advanced Very High Resolution Radiameter. Journal of Geophysical Research, 89(D5): 7231–7237 [DOI: 10.1029/JD089iD05p07231]

Qiu J. 2008. The third pole. Nature, 454(24): 393–396

Qin Z H, Dall O G and Karnieli A. 2001. Derivation of split window algorithm and its sensitivity analysis for retrieving land surface temperature from NOAA-advanced very high resolution radiometer data. Journal of Geophysical Research, 106(D19): 22655–22670 [DOI: 10.1029/2000JD900452]

Saunders R W and Kriebel K T. 1988. An improved method for detecting clear sky and cloudy radiances from AVHRR data. International Journal of Remote Sensing, 9(1): 123–150 [DOI: 10.1080/01431168808954841]

Sobrino J A and Caselles V. 1991. A methodology for obtaining the crop temperature from NOAA-9 AVHRR data. International Journal of Remote Sensing, 12(12): 2461–2475 [DOI: 10.1080/01431169108955280]

Sobrino J A, Li Z L, Stoll M P and Becker F. 1994. Improvements in the Split-Window Technique for Land Surface Temperature Determination. Transactions on Geoscience and Remote Sensing, 32(2): 243–253

Sobrino J A, Kharraz J E and Li Z L. 2003. Surface temperature and water vapour retrieval from MODIS data. International Journal of Remote Sensing, 24(24): 5161–5182 [DOI: 10.1080/0143116031000102502]

Sobrino J A and Raissouni N. 2000. Toward Remote Sensing methods for land cover dynamic monitoring: application to Morocco. International Journal of Remote Sensing, 21(2): 353–366 [DOI: 10.1080/014311600210876]

Wan Z and Li Z. 1997. A physics-based algorithm for retrieving land-surface emissivity and temperature from EOS/MODIS data. Transactions on Geoscience and Remote Sensing, 35(4): 980–996 [DOI: 10.1109/36.602541]

Wan Z, Zhang Y, Zhang Q and Li Z L. 2004. Quality assessment and validation of the MODIS global land surface temperature. International Journal of Remote Sensing, 25(1): 261–274 [DOI: 10.1080/0143116031000116417]

王兴, 张强, 郭铌, 蔡迪花. 2007. 利用MOIDS数据判别祁连山区积雪方法研究. 干旱气象, 25(2): 29–34

武荣盛, 马耀明. 2010. 青藏高原不同地区辐射特征对比分析. 高原气象, 29(2): 251–259

Yang K, Koike T, Ishikawa H, Kim J, Li X, Liu H Z, Liu S M, Ma Y M and Wang J M. 2008. Turbulent flux transfer over bare-soil surfaces: characteristics and parameterization. Journal of Applied Meteorology and Climatology, 47(1): 276–290 [DOI: 10.1175/2007JAMC1547.1]

Yang H and Yang Z D. 2006. A modified land surface temperature split window retrieval algorithm and its applications over China. Global and Planetary Change, 52(1/4): 207–215 [DOI: 10.1016/j.gloplacha.2006.02.015]

赵英时. 2003. 遥感应用分析原理与方法. 北京: 科学出版社

朱卫军. 2008. 基于单通道算法和MODIS数据的地表温度反演研究. 城市勘测, (5): 97–100